Physics of the Earth and Planetary Interiors 270 (2017) 113–127

Contents lists available at ScienceDirect

Physics of the Earth and Planetary Interiors

journal homepage: www.elsevier.com/locate/pepi

Inversion of magnetotelluric data using integral equation approach with variable sensitivity domain: Application to EarthScope MT data

Martin Čuma [a,b,c,*], Alexander Gribenko [a,b], Michael S. Zhdanov [a,b]

[a] Consortium for Electromagnetic Modeling and Inversion, University of Utah, Salt Lake City, UT 84112, United States
[b] TechnoImaging, Salt Lake City, UT 84107, United States
[c] Center for High Performance Computing, University of Utah, Salt Lake City, UT 84112, United States

ARTICLE INFO

Article history:
Received 6 July 2016
Received in revised form 16 May 2017
Accepted 5 June 2017
Available online 15 June 2017

Keywords:
Magnetotellurics
Inversion
Integral equation
EarthScope

ABSTRACT

We have developed a multi-level parallel magnetotelluric (MT) integral equation based inversion program which uses variable sensitivity domain. The limited sensitivity of the data, which decreases with increasing frequency, is exploited by a receiver sensitivity domain, which also varies with frequency. We assess the effect of inverting principal impedances, full impedance tensor, and full tensor jointly with magnetovariational data (tipper). We first apply this method to several models and then invert the EarthScope MT data. We recover well the prominent features in the area including resistive structure associated with the Juan de Fuca slab subducting beneath the northwestern United States, the conductive zone of partially melted material above the subducting slab at the Cascade volcanic arc, conductive features in the Great Basin and in the area of Yellowstone associated with the hot spot, and resistive areas to the east corresponding to the older and more stable cratons.

1. Introduction

The MT method which images electrical conductivity provides a valuable complement to other geophysical exploration methods. USArray, a large project aiming at better understanding North American litospheric structure, includes an MT component called EMScope, managed by Oregon State University on behalf of IRIS. By the end of 2011, long-period MT data had been collected at 330 stations over the north-western US. Several groups, including ours, have presented their preliminary interpretations using full impedance tensor data (Patro and Egbert, 2008; Zhdanov et al., 2011, 2012; Bedrosian and Feucht, 2013) as well as more in depth interpretation using full impedance tensor plus tipper (Meqbel et al., 2013), which largely correlate well with features revealed by seismic methods.

MT inversion is challenging due to time demand of the 3D forward modeling and the non-uniqueness of the inverse problem. Traditional methods of inversion of electromagnetic (EM) data are based on using the finite-difference (FD), finite-volume (FV), or finite-element (FE) forward modeling techniques, which are usually considered as the most powerful methods of solving Maxwell's equations. However, there exists an alternative approach for modeling geophysical EM data, based on integral equaiton (IE) method. It was introduced originally in a pioneering paper by Dmitriev (1969), which was published in Russian and long remained unknown to western geophysicists (as well as the work of Tabarovsky (1975)). More than 30 years ago, practically simultaneously, Raiche (1974), Weidelt (1975) and Hohmann (1975) published their famous papers on the IE method. Since that time, many more researchers have contributed to the improvement and development of this method (e.g., Wannamaker, 1991; Xiong, 1992; Avdeev et al., 2002; Hursán and Zhdanov, 2002; Abubakar and van den Berg, 2004 just to mention a few). It was demonstrated in these and many other publications that not only IE method can compete with the FD and FE methods in the number of the discretization cells, but there are several advantages in using the IE method in the EM modeling and inversion in comparison with the more traditional FD and FE approaches. First, the entire 3D earth model need not be discretized with an appropriate choice of boundary conditions so as to emulate an unbound 3D earth model. Rather, an appropriate background conductivity model is chosen, and only the volume of interest is discretized, with all boundary conditions perfectly matched. Second, IE forward modeling requires the calculation of the Green's tensors for the background conductivity model. These tensors can be precomputed only once and saved for multiple use on every iteration of inversion, which speeds up the computation of the predicted data on each iteration significantly. Third, the same precomputed Green's

* Corresponding author.
E-mail address: m.cuma@utah.edu (M. Čuma).

http://dx.doi.org/10.1016/j.pepi.2017.06.003
0031-9201/

tensors can be readily used for Frechet derivative calculations, which is another important element of inversion. Finally, one can exploit the fact that the area of the sensitivity of the EM receiver is significantly smaller than the area of an EM survey to develop a robust 3D inversion method which uses a moving sensitivity domain (MSD) approach.

We have developed a multi-level parallel MT inversion program that uses the contraction integral equation (CIE) approach (Hursán and Zhdanov, 2002) for forward modeling and regularized reweighted conjugate gradient (RRCG) method for the inversion (Zhdanov, 2002, 2015). Due to decreasing sensitivity of the electromagnetic (EM) fields with distance, we utilize the moving sensitivity domain approach which results in significant performance improvements. We have incorporated frequency dependent variable sensitivity and evaluated the inversion approach on different data combinations, including principal impedances only, full impedance tensor, tipper (magnetovariational – MV tensor), and full impedance tensor jointly with tipper. This paper presents the results of interpretation of the EarthScope MT data using the developed multi-level parallel magnetotelluric (MT) inversion code based on integral equation method and a variable sensitivity domain approach.

2. Forward modeling using integral equation method with inhomogeneous background conductivity

In MT methods, the earth's natural electromagnetic field is used as a source field. The mutually orthogonal horizontal components of electric and magnetic fields are recorded on the earth's surface. The interpretation of magnetotelluric data is based on the calculation of the transfer functions between the horizontal components of the electric and magnetic fields, which form the *magnetotelluric impedance tensor*:

$$\widehat{\mathbf{Z}} = \begin{bmatrix} Z_{xx} & Z_{xy} \\ Z_{yx} & Z_{yy} \end{bmatrix}. \tag{1}$$

Another important transfer function relates the vertical component of the magnetic field, H_z, and the horizontal components, H_x and H_y, as follows:

$$H_z = T_{zx}H_x + T_{zy}H_y, \tag{2}$$

where vector $T = [T_{zx}, T_{zy}]$ is called a tipper.

The expressions for the components of the full impedance tensor and a tipper can be found, for example, in Berdichevsky and Zhdanov (1984).

In developing a large-scale MT inversion algorithm, we use the integral equation (IE) method as the main engine for forward modeling. In the framework of this method, the EM field is presented as a sum of the background, $\left\{\mathbf{E}^b, \mathbf{H}^b\right\}$, and anomalous, $\{\mathbf{E}^a, \mathbf{H}^a\}$, fields:

$$\mathbf{E} = \mathbf{E}^b + \mathbf{E}^a, \quad \mathbf{H} = \mathbf{H}^b + \mathbf{H}^a, \tag{3}$$

where the background field is a field generated by the given sources in the model with a background distribution of conductivity σ_b, and the anomalous field is produced by the anomalous conductivity distribution $\Delta\sigma(\mathbf{r}), \mathbf{r} \in D_a \subset R^3$.

We should note, however, that the main limitation of the conventional IE method is that the background conductivity model must have a simple 1D structure to allow for an efficient Green's function calculation. In many practical applications, however, it is difficult to describe a model using horizontally layered background conductivity. As a result, the domain of integration may become too large, which increases significantly the size of the modeling domain and of the required computer memory and computational time for IE modeling.

It was demonstrated in Zhdanov et al. (2006) that one can overcome these computational difficulties by using the model with an inhomogeneous background conductivity (IBC). In this case, we consider a 3D geoelectrical model with horizontally layered (normal) conductivity, σ_n, inhomogeneous background conductivity, $\sigma_b = \sigma_n + \Delta\sigma_b$, within a domain D_b, and anomalous conductivity, $\Delta\sigma$, within a domain D_a. The IBC method is based on the separation of the fields, $\left\{\mathbf{E}^{\Delta\sigma_b}, \mathbf{H}^{\Delta\sigma_b}\right\}$, due to excess electric current, $\mathbf{j}^{\Delta\sigma_b} = \Delta\sigma_b\mathbf{E}$, induced in the inhomogeneous background domain D_b from the fields, $\left\{\mathbf{E}^{\Delta\sigma}, \mathbf{H}^{\Delta\sigma}\right\}$, due to the anomalous electric current, $\mathbf{j}^{\Delta\sigma} = \Delta\sigma\mathbf{E}$, in the location D of the anomalous conductivity, respectively. As a result, we arrive at a system of integral equations which uses the same simple Green's functions for the layered model with conductivity σ_n, as in the conventional IE formulation. However, the new equations take into account the effect of the variable background conductivity distribution (Zhdanov et al., 2006; Zhdanov, 2009; Endo et al., 2008).

Then, the electric and magnetic fields can be obtained by the following integral equations:

$$\mathbf{E}(\mathbf{r}') - \mathbf{E}^b(\mathbf{r}') = \iiint_{D_a} \mathbf{G}_E(\mathbf{r}', \mathbf{r})\Delta\sigma\mathbf{E}(\mathbf{r})d\nu = \mathbf{G}_E^{D_a}(\Delta\sigma\mathbf{E}), \tag{4}$$

$$\mathbf{H}(\mathbf{r}') - \mathbf{H}^b(\mathbf{r}') = \iiint_{D_a} \mathbf{G}_H(\mathbf{r}', \mathbf{r})\Delta\sigma\mathbf{E}(\mathbf{r})d\nu = \mathbf{G}_H^{D_a}(\Delta\sigma\mathbf{E}), \tag{5}$$

where $\mathbf{G}_E$ and $\mathbf{G}_H$ are the electric and magnetic Green's tensors for a layered model with conductivity σ_n.

In Eqs. (4) and (5), the symbols $\mathbf{G}_E^{D_a}$ and $\mathbf{G}_H^{D_a}$ denote the electric and magnetic Green's operators with a volume integration of D_a, respectively.

The process of solving the forward electromagnetic problem according to Eqs. (4) and (5) consists of two parts. First, it is necessary to find the electric and magnetic fields inside domain D_a (where $\Delta\sigma_a \neq 0$), which requires the solution of an integral equation (*domain equation*) (4) for $\mathbf{r}' \in D_a$. Solution of this equation exists and is unique, as solution of Fredholm equation of the second kind. Second, using the *data equations*, (4) and (5), with $\mathbf{r}' \in P$, we calculate the EM field in the receiver's domain P. Usually, the first part is more complicated and requires most of the computational time, because it consists of solving a large system of linear equations.

The domain equation in numerical dressing is reduced to a linear system of equations,

$$(\mathbf{I} - \mathbf{G}\,\mathbf{m})\mathbf{E} = \mathbf{E}^{\mathbf{b}}, \tag{6}$$

where $\mathbf{m}$ is a matrix of the anomalous conductivities of the model determined on some discretization grid, $\mathbf{I}$ is the identity matrix, $\mathbf{G}$ is the matrix of volume integrated Green's tensors for the background conductivity model, $\mathbf{E}$ and $\mathbf{E}^{\mathbf{b}}$ are the vectors of the total and background electric fields, respectively.

Following Hursán and Zhdanov (2002) and Zhdanov (2002, 2009, 2015), we use the contraction integral equation (CIE) method, which is based on preconditioning Eq. (6) with contraction operators to improve the conditioning of the matrix system.

The system of linear equations of CIE method can be written in the form:

$$\mathbf{E}_{pr}^b = \mathbf{C}\mathbf{E}_{pr}, \tag{7}$$

where $\mathbf{E}_{pr}^b$ is a vector of preconditioned background electric field, $\mathbf{E}_{pr}$ is a vector of preconditioned total electric field in the anomalous conductivity domain, and $\mathbf{C}$ is a matrix of CIE equations.

We use the Complex Generalized Minimal Residual (CGMRM) method as a solver of the system of linear equations arising in

the CIE method (Zhdanov, 2002, 2015). Note that, a linear operator, represented by matrix **C** of CIE equations, is an absolutely positively determined (APD) linear continuous operator, which, according to the convergence theorem for the CGMRM method, ensures the convergence of the CGMRM algorithm for arbitrary conductivity models. The computed electric and magnetic field are then used to determine the MT impedance.

The matrix **C** of the forward operator (7) is formed by a product of the corresponding preconditioners and the matrices of Green's operators $\mathbf{G}_E^{D_a}$ and $\mathbf{G}_H^{D_a}$ acting within the anomalous domain (Zhdanov, 2002, 2009, 2015). It has been shown by Hursán and Zhdanov (2002), that if the anomalous domain is discretized into a horizontally homogeneous array of cells, then the matrices of Green's operators have a block Toeplitz structure meaning that we could perform multiplications of the translationally invariant horizontal components of matrix **C** without needing to store its full size. Indeed, in this case the number of different entries for storing matrices of Green's operators $\mathbf{G}_E^{D_a}$ and $\mathbf{G}_H^{D_a}$ is much less than the total number of elements of the matrix, providing a good opportunity for economic storage. Moreover, this property provides an effective computational tool as well. It can be shown that the multiplication with the preconditioned matrix **C** can be represented as a sequence of discrete 2D convolutions, followed by summation over the third (vertical) coordinate.

The matrix Eq. (7) can be written in scalar notations as follows:

$$E^b_{\alpha i} = \sum_{\beta=x,y,z}\sum_{n=1}^{N_z}\left(C_{\alpha i\beta n} * E_{\beta n}\right), \quad \alpha = x,y,z; \quad i = 1,\ldots,N_z; \tag{8}$$

where, $C_{\alpha i\beta n}$ is an array of matrix **C** kernels (the array storing all different nonzero scalar components of **C**); α and β are the indices of the corresponding scalar components of the vectors $\mathbf{E}^b_{pr}$ and $\mathbf{E}_{pr}$, respectively (x, y, and z components respectively); i and n are the indices of the source and receiver positions along the vertical axis z in the expression for the Greens tensor; and asterisk "$*$" denotes a discrete 2D convolution in the horizontal plane XY. We can apply the discrete convolution theorem:

$$C_{\alpha i\beta n} * E_{\beta n} = FFT^{-1}\left[FFT(C_{\alpha i\beta n}) \cdot FFT(E_{\beta n})\right]. \tag{9}$$

The advantage of using this equation is that we replace the direct matrix multiplication with the fast Fourier transforms, reducing the operation complexity from $O(N^3)$ to $O(N^2 logN)$, where $N = N_x \times N_y \times N_z$.

This forward modeling approach is implemented as a parallel application with two nested levels of Message Passing Interface (MPI) parallelization and an additional OpenMP threading inside of each MPI process. On the MPI level, the higher level parallelization goes over the frequencies of the MT field, the lower over the horizontal layers of the 3D modeling domain. The fields and impedances calculated for each frequency are independent of each other, so there is no need for MPI communication in the modeling stage at the frequency parallelization level.

The domain parallelization level requires parallel distribution of the operation in Eq. (9), which is the most computationally demanding part of the forward modeling problem. The matrix **C** and vector $\mathbf{E}_{pr}$ are distributed using one-dimensional block cyclic distribution. We thus store only local parts of the matrix **C** and vectors $\mathbf{E}_{pr}$ and $\mathbf{E}^b_{pr}$ on each process. The inner product in Eq. (9) is then a parallel matrix- vector multiplication, where the vector $\mathbf{E}_{pr}$ has to be globally allgathered to perform a multiplication on the local matrix **C**, resulting in local vector $\mathbf{E}^b_{pr}$. The whole operation is also locally tiled for better cache memory utilization. The Allgather operation is very demanding on the inter-processor communication and can become a bottleneck of the algorithm. We alleviate the time impact of the Allgather in part by overlapping communication of the field vector $\mathbf{E}_{pr}$ with the computation of the matrix–vector product for a previous Z layer, using non-blocking version of the Allgather. Nevertheless, for domains of the size used in this paper(several millions of cells), parallel efficiency deteriorates beyond about 16 processes. This is where the multi-level parallel implementation becomes crucial for efficient performance. We typically run two MPI processes per cluster node, with each process using as many OpenMP threads as there are CPU cores, so one frequency can be efficiently calculated using 8 cluster nodes. With multiple MT frequencies, this allows us to run the forward modeling and inversion efficiently on hundreds of cluster nodes and thousands of CPU cores. The numerical algorithm described above is implemented in the IE based forward modeling code PIE3D (Cuma et al., 2013) developed by the Consortium for Electromagnetic Modeling and Inversion at the University of Utah.

3. Inversion of MT data

We can describe the inverse MT problem by an operator equation:

$$\mathbf{d} = \mathbf{A}(\mathbf{m}), \tag{10}$$

where **d** stands for a *data vector* formed by the components of the MT impedances, and **A** is the nonlinear forward operator symbolizing the governing equations of the MT modeling problem. We call Eq. (10) an *impedance equation*. The impedance equation is ill posed, i.e., the solution can be nonunique and unstable. We use Tikhonov regularization to solve ill-posed MT inverse problem, which is based on minimization of the following parametric functional (Tikhonov and Arsenin, 1977; Zhdanov, 2002, 2015):

$$P^\alpha(\mathbf{m}) = \|\mathbf{W}_d(\mathbf{A}(\mathbf{m}) - \mathbf{d})\|^2_{L_2} + \alpha s(\mathbf{m}), \tag{11}$$

where $\varphi(\mathbf{m}) = \|\mathbf{W}_d(\mathbf{A}(\mathbf{m}) - \mathbf{d})\|^2_{L_2}$ is the misfit functional between the predicted data, $\mathbf{A}(\mathbf{m})$, and the observed data **d**; $\mathbf{W}_d$ is the data weighting matrix; $s(\mathbf{m})$ is a stabilizing functional; and α is a regularization parameter.

The minimization of the parametric functional introduces a trade-off between fitting the observed data and restricting the search for the solution to some class of models having special physical and/or mathematical properties, determined by selection of a stabilizing functional, $s(\mathbf{m})$. When α is big, the stabilizing term plays the main role, and the requirement to make the misfit as small as possible is more relaxed. Conversely, when α is small, one of the best-fitting models will be found – but there could be no guarantee that this model will be unique and will have a reasonable physical meaning. This fact is due to the ill-posedness of the inverse problem. That is why the stabilizer is chosen in a special way, in order to select a solution of the inverse problem from a class of modles with specific properties.

There are different kinds of stabilizers, and each will approximate our inverse-problem operator with the use of different sets of well-posed operators. The main goal of choosing the stabilizer is to build an efficient method for constructing a solution of the ill-posed inverse problem. That is why the most frequent choice is the minimum norm stabilizer s_{MN}, which is is a quadratic functional:

$$s_{MN} = \|\Delta\sigma\|^2_{L_2} = \iiint_{D_a} |\Delta\sigma|^2 dv. \tag{12}$$

With relatively large values of α, the stabilizing term dominates the whole parametric functional, and it can be considered as a convex. The advantage of having the convex functionals is that they are characterized by a unique global minimum, which is easy to find using conventional deterministic gradient-type minimization

algorithms. It should be noted that the solution, found by using the minimum norm stabilizing functional, described above, is a smooth image of the true conductivity distribution. In many practical applications, and especially in mineral exploration, a smooth distribution of unknown parameters (e.g., conductivity) does not describe the examined object properly. In this situation, focusing stabilizers are used to produce a sharp and focused image of the mineral deposit. To summarize, Tikhonov regularization provides us with a method for finding a stable solution within different subsets of possible solutions with the specific pre-selected properties, e.g., smoothness or sharpness of invere images.

We solve the problem of minimization of Tikhonov parametric functional using the regularized conjugate-gradient (RCG) method with adaptive regularization parameter selection (Zhdanov, 2002, 2015). The RCG algorithm is based on iterative updates of the conductivity model $\mathbf{m}_n$ so as to minimize the functional $P(\mathbf{m})$:

$$\begin{aligned}
&\mathbf{r}_n = A(\mathbf{m}_n) - \mathbf{d},\\
&\mathbf{l}_n = \mathbf{l}(\mathbf{m}_n) = \mathbf{F}_n^{\dagger}\mathbf{W}_d^{\dagger}\mathbf{W}_d\mathbf{r}_n + \alpha\mathbf{W}_m^{\dagger}\mathbf{W}_m(\mathbf{m}_n - \mathbf{m}_{apr}),\\
&\beta_n = \|\mathbf{l}_n\|^2/\|\mathbf{l}_{n-1}\|^2, \quad \tilde{\mathbf{l}}_n = \mathbf{l}_n + \beta_n\tilde{\mathbf{l}}_{n-1}, \ \tilde{\mathbf{l}}_0 = \mathbf{l}_0,\\
&k_n = \left(\tilde{\mathbf{l}}_n, \mathbf{l}_n\right) \Big/ \left\{\left\|\mathbf{W}_d\mathbf{F}_n\tilde{\mathbf{l}}_n\right\|^2 + \alpha\left\|\mathbf{W}_m\tilde{\mathbf{l}}_n\right\|^2\right\},\\
&\mathbf{m}_{n+1} = \mathbf{m}_n - k_n\tilde{\mathbf{l}}_n.
\end{aligned} \tag{13}$$

where k_n is a length of the iteration step; $\mathbf{W}_m$ is the model weighting matrix; $\mathbf{l}_n$ is the gradient direction, computed using the adjoint Fréchet derivative matrix, $\mathbf{F}_n^{\dagger}$; and star denotes the adjoint operator (matrix).

The appropriate selection of the data and model weighting matrices is very important for the success of the inversion. We will discuss a selection of data weights below. Computation of the model weighting matrix is based on sensitivity analysis. In this paper we select $\mathbf{W}_m$ as the square root of the sensitivity matrix in the initial model:

$$\mathbf{W}_m = \sqrt{\mathbf{diag}(\mathbf{F}_0^{\dagger}\mathbf{F}_0)^{\frac{1}{2}}}. \tag{14}$$

As a result, we obtain a uniform sensitivity of the data to different model parameters (Zhdanov, 2002, 2015).

In the case of focusing stabilizers, we use the re-weighted regularized conjugate gradient (RRCG) method introduced in Zhdanov (2002), p. 161–166. This algorithm is similar to RCG algorithm (13). However, the inversion is conducted in the space of the weighted model parameters $\mathbf{m}_n^w$, which are related to the original parameters by the formula:

$$\mathbf{m}_n^w = \mathbf{W}_m\widetilde{\mathbf{W}}_{en}\widetilde{\mathbf{m}}_n. \tag{15}$$

In the framework of this approach, the variable weighting matrix $\widetilde{\mathbf{W}}_{en}$ is precomputed on each iteration, based on the values $\mathbf{m}_n$, obtained on the previous iteration. This linear transformation is updated every several iterations, which is equivalent to the re-weighting of the model parameters. In other words, a set of linear transformations with the repeatedly updated weighting matrices is applied to transform the non-quadratic functional into the quadratic stabilizer similar to a minimum norm stabilizer (12). We refer the interested readers to the books on inversion theory by Zhdanov (2002, 2015) for in-depth explanation of the RRCG technique, which is widely used now in different geophysical applications.

In expression (15) we use the logarithmic model parameters, vector $\widetilde{\mathbf{m}}$, with the scalar components $\widetilde{m}_i$ given by the formula:

$$\widetilde{m}_i = \ln\left(\frac{\Delta\sigma_i - \Delta\sigma_i^-}{\Delta\sigma_i^+ - \Delta\sigma_i}\right). \tag{16}$$

This log parameterization has a property that the scalar components of the original conductivity vector $\Delta\sigma$ always remain within the given lower and upper bounds $\Delta\sigma_i^-$ and $\Delta\sigma_i^+$:

$$\Delta\sigma_i^- \leqslant \Delta\sigma_i \leqslant \Delta\sigma_i^+, \ i = 1, 2, \ldots .L. \tag{17}$$

We apply the *adaptive* regularization method. The regularization parameter α is updated in the process of the iterative inversion as follows:

$$\alpha_n = \alpha_1 q^{n-1}; \ \ n = 1, 2, 3 \ldots ..; \ 0 < q < 1. \tag{18}$$

In order to avoid divergence, we begin an iteration from a value of α_1, which can be obtained as a ratio of the misfit functional and the stabilizer for an initial model, then reduce α_n according to formula (18) on each subsequent iteration and continuously iterate until the misfit condition is reached:

$$r_{n0}^w = \left\|\mathbf{r}_{n0}^w\right\| = \|\mathbf{W}_d\left(\mathbf{A}\left(\mathbf{m}_{\alpha_{n0}}\right) - \mathbf{d}\right)\|/\|\mathbf{W}_d\mathbf{d}\| = \delta, \tag{19}$$

where r_{n0}^w is the normalized weighted residual, and δ is the relative level of noise in the weighted observed data.

Parameter q controls the rate of the regularization parameter decrease in the process of inversion. This parameter is usually selected within an interval [0.5; 0.9]. This allows the inversion model to depart more freely from the a priori model as the misfit decreases.

At each iteration, computation of the sensitivities for an entire MT survey is needed, which is computationally challenging problem. We solve this by using quasi-Born approximation (Zhdanov, 2009), which reduces the number of computations dramatically while retaining a numerically stable solution.

The Fréchet derivative is the most expensive item in the inversion not only in terms of the computation time, but also in the computer memory required for its storage. The number of entries in the Fréchet derivative matrix is equal to the number of MT data points times the number of cells in the inversion domain. With large amounts of data and vast inversion regions, the computer memory requirements may become prohibitive. To reduce the storage requirements, we use a moving sensitivity domain (MSD) approach in our MT inversion (Cox et al., 2010).

In the framework of the MSD approach, for a given receiver we compute and store the Fréchet derivative inside the inversion cells within a predetermined horizontal distance from this receiver only; i.e., within a sensitivity domain. Thus, Fréchet derivatives for an MT station can be computed and stored only for regions much smaller than the entire inversion domain, resulting in dramatic reduction of the computer memory requirements. The sensitivity domain size is determined based on the rate of sensitivity attenuation of MT data. As the sensitivity attenuates faster for higher frequencies, we vary the sensitivity domain size with frequency, which provides the optimal memory and computation use while retaining maximum accuracy. We apply the MSD approach for the Fréchet derivative calculation and not for the computations of the predicted field. By using all of the cells in the forward modeling computations, we ensure an accurate result for the calculations of the predicted fields in the receivers.

MT data accuracy may vary from station to station, and with frequency. At the same time, we observe significant noise in the very low frequency range of the EMScope MT data due to longer time periods needed to collect statistically significant measurements. The signal strength also increases with frequency. It is thus advisable to include both the strength of the signal and an accuracy information into the inversion process in order to weigh each data point accordingly. We utilize an approach similar to Avdeev and Avdeeva, 2009, where we include the covariance of the measured data in the data weights as follows:

$$W_{d,jn} = \frac{1}{\beta_{jn}\|\mathbf{Z}\|\sqrt{f}}, \tag{20}$$

where f is the frequency, and the impedance norm is computed over each impedance component for all the stations and frequencies; β_{jn} is the relative error of the observed impedance Z_{jn} defined as

$$\beta_{jn} = \sqrt{\frac{\varepsilon_{jn}}{Z_{jn}^{T} Z_{jn}}}, \tag{21}$$

and ε_{jn} is the reported impedance variance (j and n are the impedance matrix component indices). We should note that, the conventional approach to computing the data weights is based on using the error estimates produced by processing, which include data error floors, calculated as an average of the principal impedances. This can upweight stations where the principal impedance values for the given station are small. Our approach attempts to reduce these potentially non-desirable upweights. These data weights are then utilized in the calculation of the data weighting matrix:

$$\mathbf{W}_d = \mathbf{diag}\left[W_{d,jn}\right].$$

The parallel implementation of the 3D MT inversion is based on the forward modeling parallelization described above. There are two nested levels of MPI paralelization over the frequencies and the inversion domain along with OpenMP threading inside of each process. The inversion involves mostly reduction operations of the various properties (sensitivities, impedances, etc.), which communication impact is minimal. The performance of the parallel inversion program thus reflects that of the forward modeling code detailed above, and is described in detail in the Supplementary Information.

4. Validation of the inversion approach

We have assessed the reliability of our inversion approach on numerous models. For the sake of brevity we show a checkerboard test with $3 \times 3 \times 3$ rhomboidal 1000 or 10 Ohm-m anomalies embedded in a 100 Ohm-m background (Fig. 1). MT receivers are spaced on a 70 km grid, and, we use 24 frequencies with periods from 19.7 to 7300 s, similar to the EarthScope data. A 3% gaussian noise was added to the electromagnetic fields before calculating the impedances. We have inverted this model using principal impedances, full impedance tensor, tipper, and full impedance tensor plus tipper.

Fig. 2 shows the horizontal and vertical cross section of the inversion results. We can see that the inversion recovers the first anomaly layer quite well. In the second layer, the conductors show up very well while the resistors do not, due to higher sensitivity of the MT method to conductors and shielding of the electromagnetic currents by the upper conductors. The deepest anomaly layer shows just a hint of the conductor between 200 and 350 km depth, demonstrating the limit of the MT method at the given frequency range. The inversion of principal impedances shows a resistive echo above the uppermost conductor. The reason for this echo may be related to limited 3D sensitivity of the principal impedances. The independent tipper inversion also performs well because the background is the same as what was used for modeling. The best result is obtained with the inversion of the full impedance tensor plus tipper, which combines the strengths of the spatial resolution of the full impedance tensor with the better depth sensitivity of the tipper.

In order to evaluate the optimal size of the MSD, we use the aforementioned model data and vary the maximum MSD as a multiple of the skin depth at that frequency for the background resistivity of 100 Ohm-m. Fig. 3 shows the horizontal cross section at 50 km depth of the model obtained by inversion of the full impedance tensor. We set the sensitivity domain radius equal to the skin depth times a multiplier from 1 to 5. Notice that, the $1\times$ skin depth sensitivity domain result is very grainy and unusable. The final misfit is $1.7\times$ larger than that of the inversion result with no sensitivity domain. The result with $2\times$ skin depth sensitivity domain radius is better but there are still artifacts. The final misfit is $1.11\times$ larger than the misfit of the inversion with no sensitivity domain. The results with $3\times$ and larger skin depth sensitivity domain radius are very close to indistinguishable from the result with no sensitivity domain. The $3\times$ skin depth sensitivity domain inversion misfit is just $1.009\times$ larger than misfit of inversion with no sensitivity domain. Increasing the sensitivity domain radius to $4\times$ and $5\times$ the skin depth does not bring any further improvement. We therefore conclude that the optimal sensitivity domain radius is $3\times$ the size of the skin depth. It is also advisable to set minimum and maximum sensitivity domain radii. High frequencies with small skin depth may result in sensitivity domain that covers only a handful of horizontal cells. A very low frequency sensitivity domain may cover a very large area but with very limited sensitivity and large uncertainty due to small value of the low frequency response. In the EarthScope data inversions, we set the minimum and maximum sensitivity domain sizes to 100 km and 600 km,

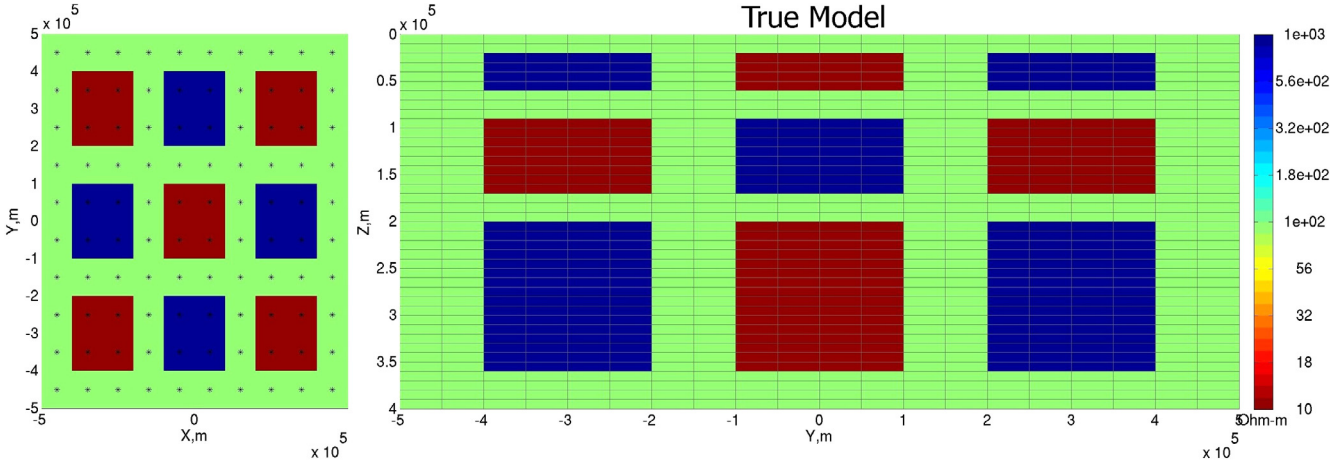

Fig. 1. Horizontal cross sections of the model at 50 km depth (left) and vertical cross sections of the same model at the center (right).

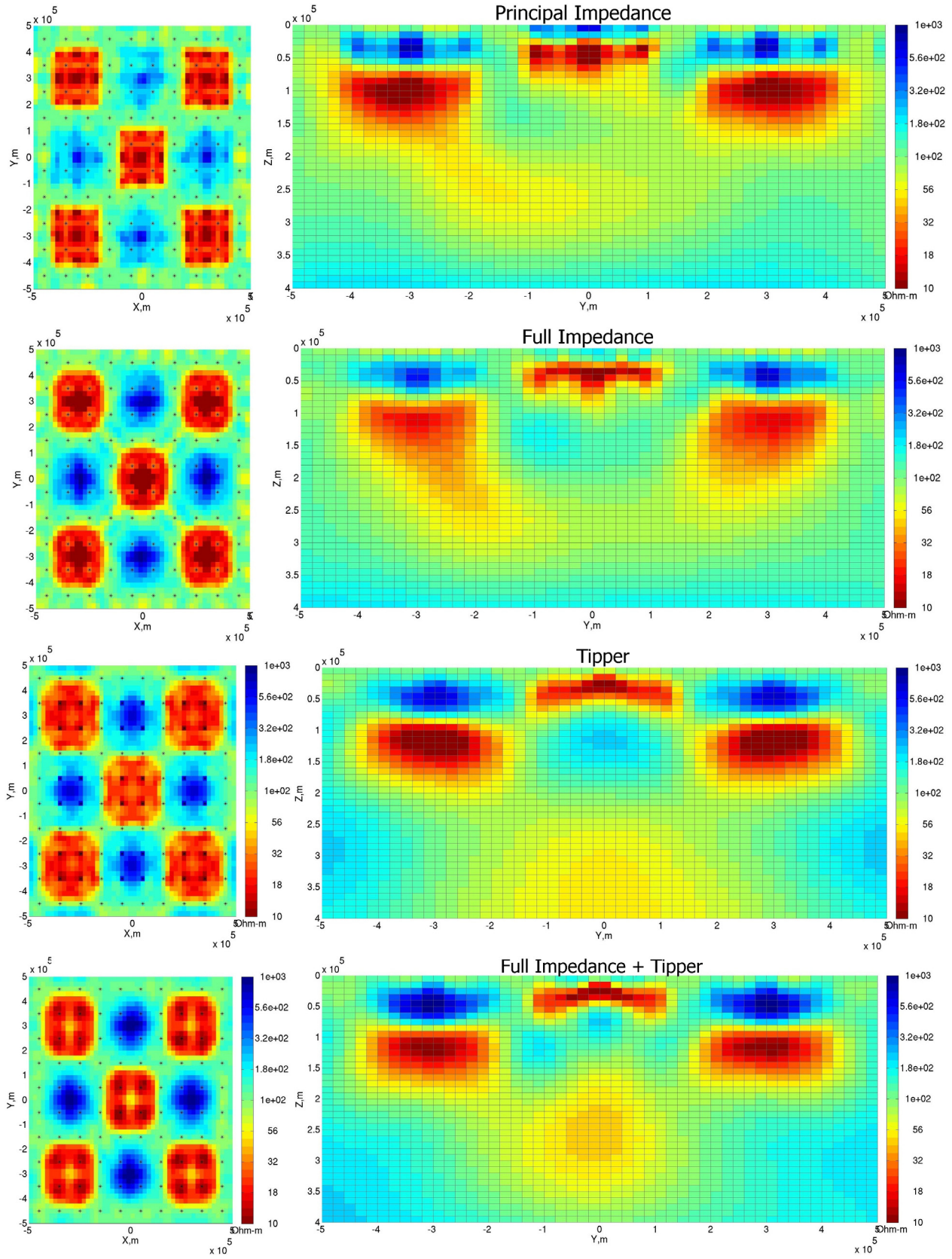

Fig. 2. Horizontal cross sections of the inversion results at 50 km depth (left) and vertical cross sections of the same model at the center (right).

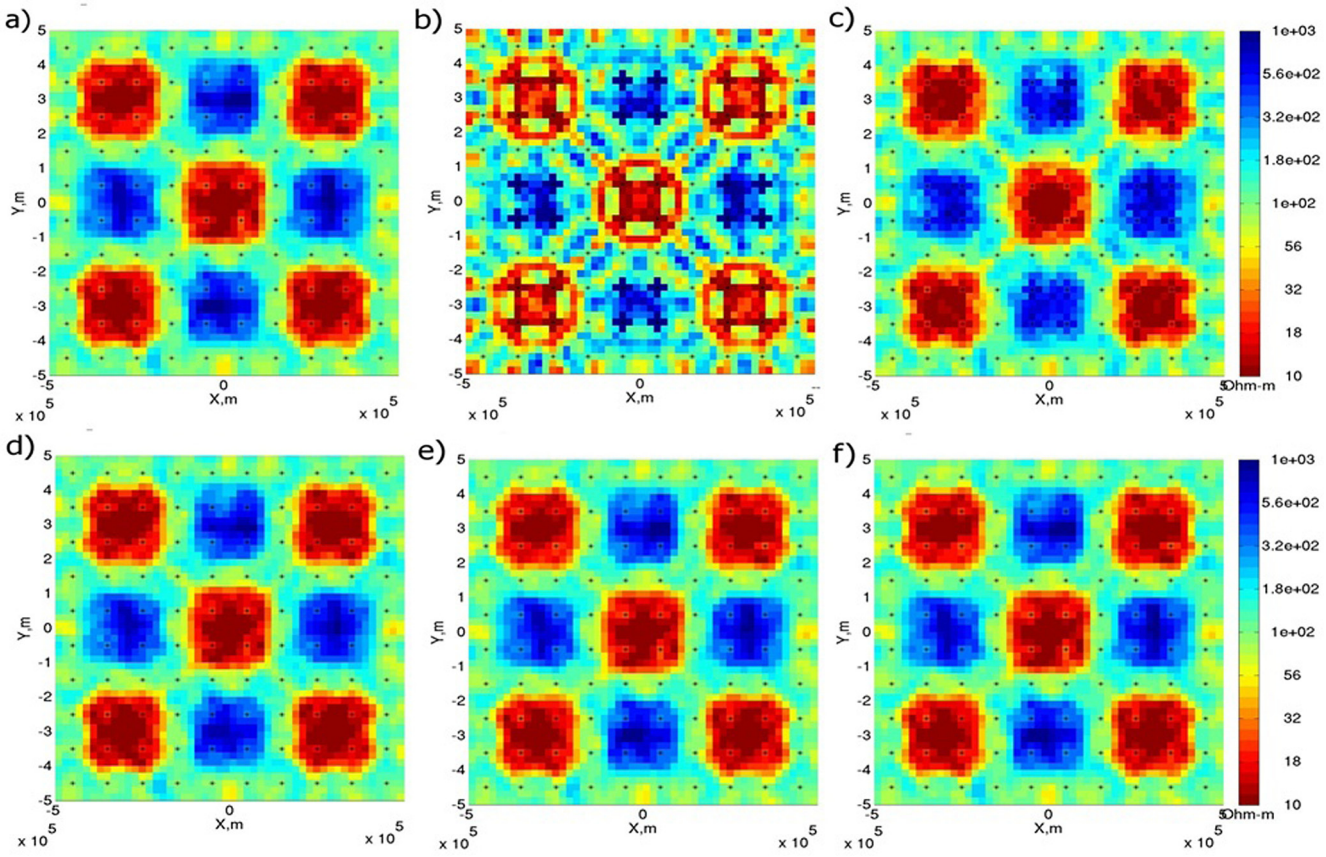

Fig. 3. Horizontal cross sections of inverted Model 1 at 40 km depth: a) no MSD, b) MSD radius of the size of skin depth, c) MSD radius 2× the size of skin depth, d) MSD radius 3× the size of skin depth, e) MSD radius 4× the size of skin depth, f) MSD radius 5× the size of skin depth.

respectively, which we have determined to be optimal from a series of coarse grid EarthScope data inversions.

5. Inversion of EarthScope MT data collected over the northwestern United States

The magnetotelluric (MT) component of the USArray program, which is an important part of the EarthScope project, is managed by Oregon State University on behalf of IRIS. We have analyzed EarthScope MT data collected in 330 stations over the northwestern United States. The station coverage extends from about 123°W to 105°W and from about 38°N to 49°N. The MT data contain four components of the impedance tensor, as well as two components of the magnetic tipper, with error variances provided for all data points. The data quality is very good overall; however, there is a handful of stations of questionable quality and some of the data, especially for the lowest and highest frequencies, have relatively large errors. We should note that, in a general case, the high frequency data are more noisy than the lower frequency data; however, for a very low frequencies, considered in the EMScope project, the limited period of observation could result in the loss of accuracy as well.

We used two-stage filtration approach in an attempt to reject the noisy data. First, we removed a few MT stations which had a very large variation of apparent resistivity or phase angle over the frequencies. Then we ran an inversion on a coarse grid (with the horizontal cell size of 25 × 25 km and 48 layers vertically with cell size increasing logarithmically with the depth), and rejected data which misfit was eight times larger than the average misfit for the given frequency and impedance component. Using this approach, we removed about ten additional data points for each frequency, resulting in 314–318 stations for each frequency. We use 24 frequencies ranging from 19.7 to 7300 s, mainly because the lower and higher frequencies had considerably larger data errors and would be effectively weighted down in the inversion, if one would consider a wider range. Another practical reason for using 24 frequencies is to more efficiently map the problem onto the distributed parallel computer. At the same time, test inversions run on a smaller subset of the data with a wider frequency range did not appreciably change the result.

The considered range of periods corresponds to a skin depth of about 500 km in a 100 Ohm-m host medium. The inversion domain was spanned in the X (geographic E-W), Y (geographic N-S), and Z (vertical downward) directions, extending 1650 km, 1350 km, and 500 km, respectively. The sensitivity domain radius for each station had a maximum of 600 km and a minimum of 100 km and was set to three times the skin depth for the given frequency at a 100 Ohm-m half-pace.

Due to the ill-posedness of MT inversion, one can generate a set of equivalent inverse models, which all fit the observed data with the same accuracy (Zhdanov, 2002, 2015). That is why we ran numerous inversions with different components of MT data (e.g., full impedance tensor vs. principal impedances), data weights, regularization parameters, and discretizations of the model, in order to determine the optimal inversion parameters and to examine the robustness of the inversion results. The outcome of this process are the models presented in this paper, where we used cells with a horizontal discretization of 10 km by 10 km, and a vertical discretization of 96 layers starting at 50 m below the surface and logarithmically increasing with depth. The inversion domain contained 2,138,400 cells, and the initial model was a homogeneous 100 Ohm-m half-space.

While we earlier determined that the effects of the conductive ocean at the western edge of the inversion domain are negligible to the mantle conductors (Zhdanov et al., 2012), this may not be the case for the Cascadia Arc conductors above the subducting oceanic slabs, which are located within a few hundred kilometers from the ocean. Therefore, we included the ocean as an a known geoelectrical feature in the inversion domain, using an inhomogeneous background domain approach discussed above (Zhdanov et al., 2006; Endo et al., 2009) for the areas west of the MT inversion domain, and as an initial and a priori model inside of the MT inversion domain. This is one of advantages of the IE method, which allows the user to include all available geoelectrical information without dramatic increase of the size of the modeling domain. We constructed the ocean geoelectrical model using 1^0 global bathymetry data from the Scrips Institution of Oceanography (Smith and Sandwell, 1997). The inversion of the data generated for the model containing the ocean shows minimal differences from that obtained for the data without the explicitly included ocean. However, over the ocean the inverse model, that includes the oceanic effects, shows a considerably shallower conductor in the ocean area.

All the model studies and preliminary EarthScope data inversions were run at the Center for High Performance Computing (CHPC) of the University of Utah. However, the inversion of the field EMScope MT data, which we present below, were run on the Stampede supercomputer at the Texas Advanced Computing Center (TACC). There we used 192 sixteen-core nodes, splitting the work into 384 MPI processes, each of which ran eight OpenMP threads, to a total of 3072 cores. The inversions were run until the normalized misfit (the norm of the residual between the predicted and observed data normalized by the norm of the observed data) had decreased to about 3.5%, which required about 50 inversion iterations and took about 20 h.

Fig. 4 shows an example of the fit between the observed and predicted impedances for a mid range period 170 s, which tends to have the smaller data errors, demonstrating an excellent fit of the data. The data fit and digital geoelectrical inverse model is described in more detail in the Supplementary Information. In this figure, we present the observed and predicted values of all four components of the impedance tensor and the corresponding residuals. From these plots, one can see that the residuals are on the order of magnitude and even less smaller than the observed impedances themselves. They are also characterized by a random pattern, which is a manifestation of the fact that the regular geoelectrical features are mostly captured by the inversion.

6. Geoelectrical model of northwestern United States obtained from EMScope MT data inversion

The deep geological structure of the northwestern United States and southwestern Canada has been extensively studied by seismologists during recent years with the deployment of the National Science Foundation (NSF) EarthScope project's USArray program, managed by the Incorporated Research Institutions for Seismology (IRIS), and regional seismic networks (e.g., Xue and Allen, 2007; Roth et al., 2008;Obrebski et al., 2010, 2011). One of the objectives of these studies was imaging the extent of the subducted Juan de Fuca plate in the mantle east of the Cascades beneath Oregon, and understanding the character of its interaction with the Yellowstone hotspot plume. It was shown in these publications that the subducting Juan de Fuca slab is expressed in the seismological models as a high-velocity anomaly which dips at approximately 46° to the east and extends downward to a depth of about 400 km.

Fig. 5 shows major geologic-tectonic features of the northwestern United States overlaid on topography and bathymetry (modified from Obrebski et al., 2010). They encompass the Cascadia subduction zone, including the descending Juan de Fuca and Gorda plates, which are the remnants of the convergent plate margin spanning coastal western North America. According to modern geological and geophysical data, the Juan de Fuca plate is subducting beneath the North American plate. The estimated depth of the top of the subducting slab is shown with blue contours (labeled in

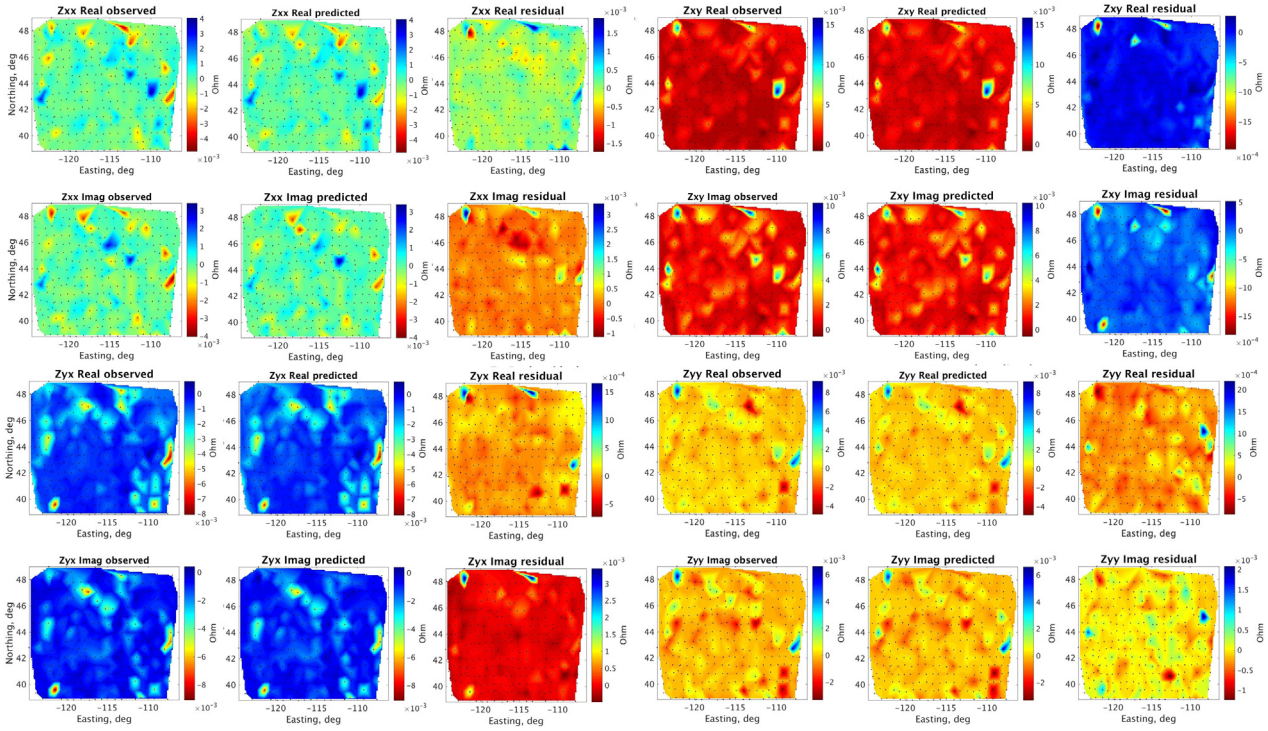

Fig. 4. Plots of the observed and predicted values for all four components of the impedance tensor and the corresponding residuals for a period of 170 s.

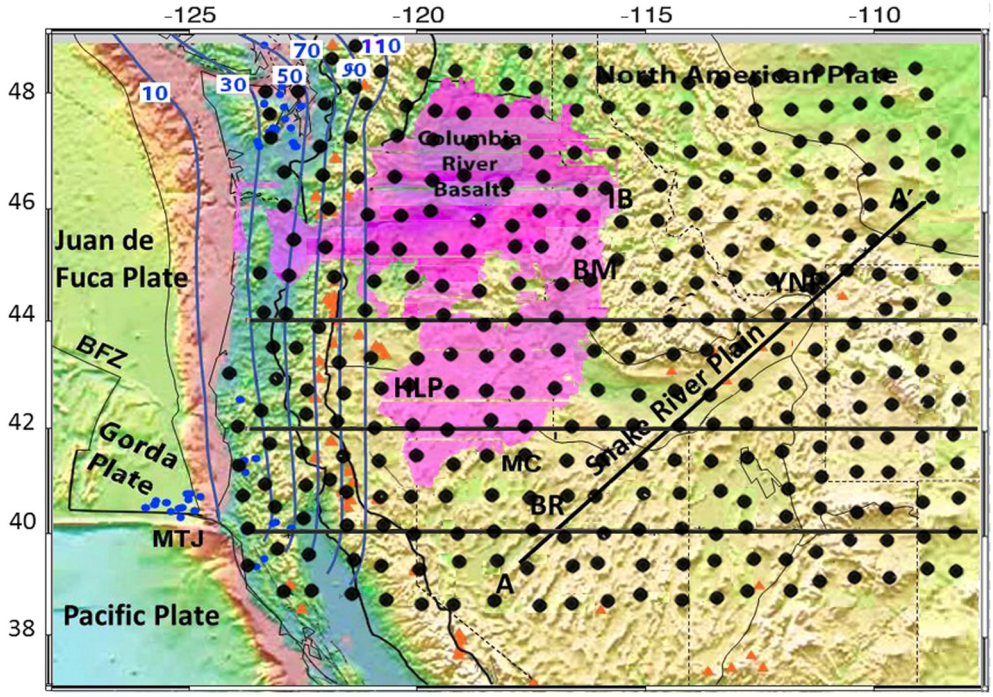

Fig. 5. Physiographic map of the northwestern United States indicating primary geologic-tectonic features (modified from Obrebski et al., 2011). BM = Blue Mountains; BFZ = Blanco Fracture Zone; BR = Basin and Range; CR = Coast Range; IB = Idaho Batholith; HLP = High Lava Plains; MTJ = Mendocino Triple Junction; YNP = Yellowstone National Park. The locations of MT stations used in the inversion are shown by black stars. (For interpretation of the references to colour in this figure caption, the reader is referred to the web version of this article.)

km) in Fig. 5. The locations of all M >4 earthquakes with depths ⩾35 km since 1970 are shown as blue dots. Volcanoes are shown as orange triangles. The Snake River Plain traces the path of the North American plate over the Yellowstone hotspot, now centered in Yellowstone National Park (YNP). The Columbia River Flood Basalt Province represents a massive outpouring of basalt from about 16.6 to 15.0 Ma and is shown in pink (Camp and Ross, 2004).

The conductivity distribution as recovered by our 3D inversion of the EarthScope MT data reflects the regional features of the northwestern United States. Figs. 6–8 compare horizontal cross sections of our geoelectrical model at depths of 80 km, 150 km and 300 km, respectively, with the seismic velocity model obtained from joint inversion of body-wave travel times and surface-wave phase velocities (Obrebski et al., 2011). The subducting Juan de Fuca slab (JDF) is clearly imaged in these horizontal sections. It is characterized by the zone of very high resistivity (∼1000 Ohm-m) shown by the dark blue color, which corresponds well to the known fact that the subducting oceanic lithosphere is very resistive (e.g., Wannamaker et al., 1989). There is also a hint of the division between the JDF Plate, Gorda Plate and Pacific Plate revealed by higher conductivity in the area of south-western Oregon.

We observe several conductive lineaments in the resistivity maps at 80 km depth, similar to those identified by Patro and Egbert (2008) and Meqbel et al. (2013). For example, conductive lineament HLP extends under the High Lava Plains to the NW toward the Blue Mountains (BM). It can be associated with the northwestward propagating High Lava Plains volcanic lineament, and it corresponds to the reduced velocity zone (RVZ) beneath the Newberry region, identified by Roth et al. (2008) from high-resolution 3D P-wave tomography. Roth et al. (2008) explained

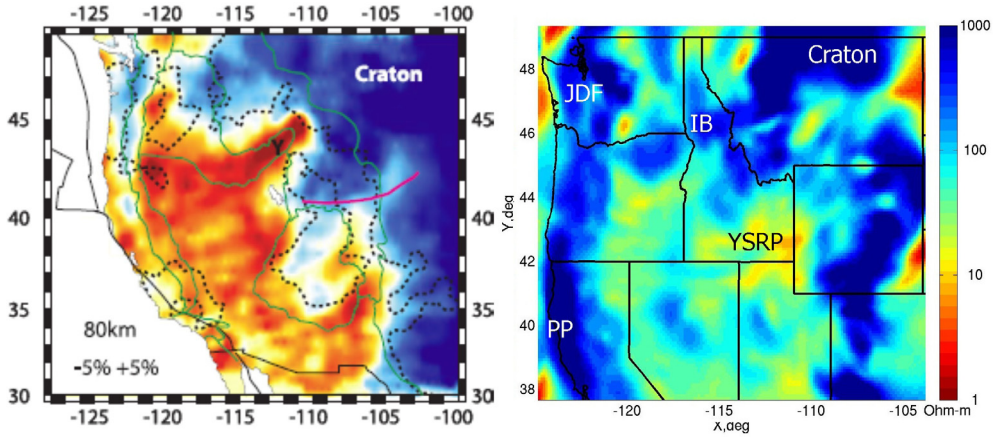

Fig. 6. Horizontal cross section at depth of 80 km obtained with joint seismic inversion (Obrebski et al., 2011) and with MT inversion

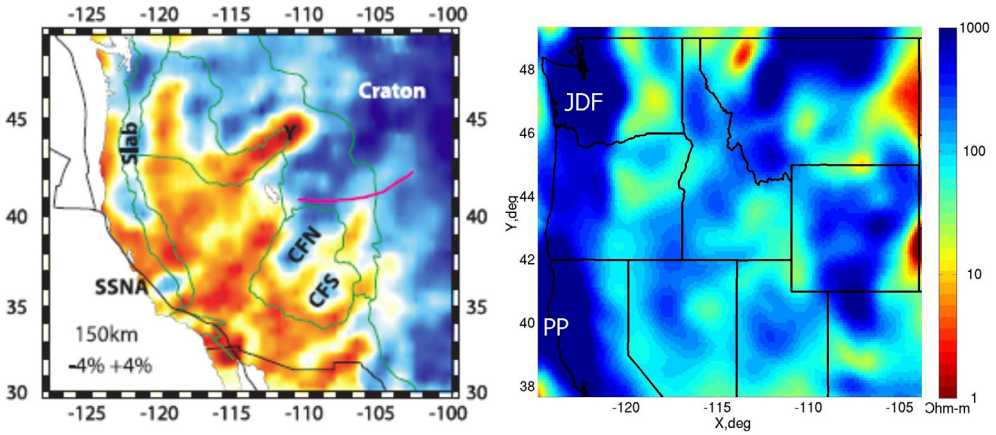

Fig. 7. Horizontal cross section at depth of 150 km obtained with joint seismic inversion (Obrebski et al., 2011) and with MT inversion.

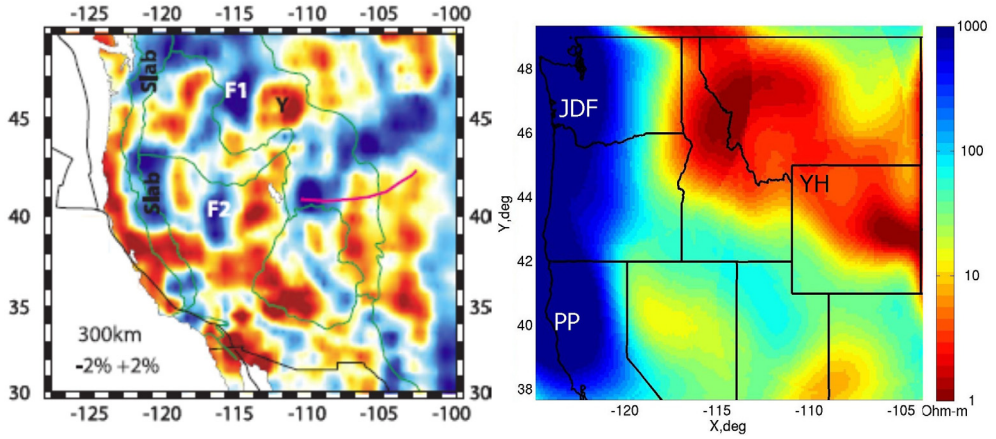

Fig. 8. Horizontal cross section at depth of 300 km obtained with joint seismic inversion (Obrebski et al., 2011) and with MT inversion.

the low-velocity anomaly beneath Newberry and the High Lava Plains by the presence of partially melted material due to the release of fluids from the downgoing slab. This partially melted material may also result in the decreased resistivity (∼5 Ohm-m), which is observed beneath the western side of the Blue Mountains. This hypothesis is supported by the geochemical characteristics of the Newberry basalts, which, according to Carlson et al. (2008) are strongly influenced by subducted slab-derived fluids. Another conductivity anomaly extends beneath the Columbia River basalts in south-central Washington (CRB). This anomaly (~5 Ohm-m) corresponds well to the reduced velocity zone identified by Roth et al. (2008) beneath the thick sections of the Columbia River basalts as related to the geothermal processes in the surrounding areas.

An important feature of our geoelectrical model is conductive lineament extending beneath the Yellowstone – Snake River Plain (YSRP). This conductive structure corresponds well to the reduced velocity anomaly within the Precambrian lithosphere identified by both Roth et al. (2008) and Obrebski et al. (2010, 2011), and is characterized by high temperatures and low density. We observe also the conductivity anomaly YSRP rising from the mantle at a depth of ∼100 – 200 km in the vicinity of Yellowstone, associated with the Yellowstone conductive plume-like layer identified by Zhdanov et al. (2011) using a subset of the EarthScope MT survey of 28 MT stations located over the area surrounding Yellowstone National Park. The highly conductive body is associated with the tomographically imaged mantle plume-like layer emerging from the upper mantle toward the Yellowstone volcano (e.g., Schutt and Dueker, 2008; Schutt et al., 2008; Schmandt and Humphreys, 2010; Waite et al., 2005; Smith et al., 2009). Similar to the slow velocity anomaly imaged by James et al. (2011), the conductive plume is in fact a mantle layer that extends in a southwest direction into eastern Idaho. This observation opens a possibility for different interpretations of Yellowstone velocity and conductivity anomaly, including tectonic models alternative to "a simple deep-mantle plume hypothesis" (e.g., Obrebski et al., 2010; Fouch, 2012).

We also observe a resistive anomaly beneath the northern Idaho close to the Idaho Batholith (IB) near the margin of Precambrian North America. Notably, this resistive zone corresponds to the region of increased (~2%) velocities described by Roth et al. (2008). However, contrary to the region of increased velocities observed by Roth et al. (2008), which extends to the somewhat unexpected depths of 400 km, the resistive zone extends to depths of up to 200 km, which seems to be more typical for the continental lithosphere. Roth et al. (2008) explain the greater than expected depth of the continental lithosphere determined by seismic data as downward smearing of the tomographic image, given the currently limited data coverage in the model for that region. Another explanation for this resistor has been recently suggested by Schmandt and Humphreys (2011), arguing that this resistor is due to a fragmented oceanic lithosphere slab that has been twisted and lifted up by subsequent Juan de Fuca plate subduction from the west. To the northeast we notice prominent resistors consistent with the Wyoming Craton (WC) and the Medicine Hat Craton (MHC).

Fig. 9 compares shallower horizontal cross sections at 35 km depth. Notice several strong conductors in the western part corresponding to the Cascadia Volcanic Arc (CVA) volcanoes (Mt. Rainer – MR, Mt. St. Helens – Mt. Adams – MA, Mt. Jefferson – MJ, Sisters - S, Mt. Shasta – MS, Lassen Pk. – LP), with the most prominent large conductor under the Mt. St. Helens – Mt. Adams complex (MA). There are also localized conductors in the Great Basin, and northern Rockies area and a prominent conductive area corresponding to the Yellowstone – Snake River Plain. Resistive features are again apparent in the northeastern cratons and under the western Colorado and central Wyoming.

We turn our attention now to vertical cross sections in Fig. 10, which along with the previously discussed horizontal section provide a 3D perspective on the geoelectrical model. We show vertical slices along 40.5 N, 44 N and 46.5 N. The subducting Juan de Fuca slab is clearly imaged by the geoelectrical model as a high-resistivity anomaly dipping east under 46.5 N. It is manifested in the P- and S-wave tomographic models of Obrebski et al. (2010, 2011) as the high-velocity anomaly which dips east under a similar angle ~46°. We also can see the conductive zone of partially melted material directly above the subducting slab, which can be explained by the release of fluids from the down-going slab. In particular, a vertical section at 46.5 N corresponds to the vicinity of Mt. Rainier and Mt. Adams, a vertical section at 44 N goes in vicinity of Sisters, and a section at 40.5 N is located in vicinity of Lassen Pk. All vertical resistivity sections show large zones of moderate-to–high conductivity (~5–10 Ohm-m) below 100–200 km in the upper mantle, which represent the electrical properties of the conductive electrical asthenosphere.

Another remarkable geoelectrical feature shown in the vertical resistivity sections is an extensive area of low resistivity (~1–10 Ohm-m) in the upper mantle, and in some parts, in the low crust, which extends beneath the northwest Basin and Range (BR), High Lava Plains (HLP) and Yellowstone-Snake River Plain (YSRP). Note that, a similar result was observed by Bedrosian and Feucht (2013) and Meqbel et al., 2013 using finite difference based 3D inversion of the EarthScope MT data. Interestingly, as early as in 1977, Stanley et al. (1977) conducted MT soundings along a profile extending from the Raft River geothermal area in southern Idaho to Yellowstone National Park in Wyoming. The 1D interpretation of these MT sounding curves revealed a highly conductive crustal anomaly with the depth of the conductive zone about 25 km and whose resistivity is less than 10 Ohm-m and at some sites less than 1 Ohm-m.

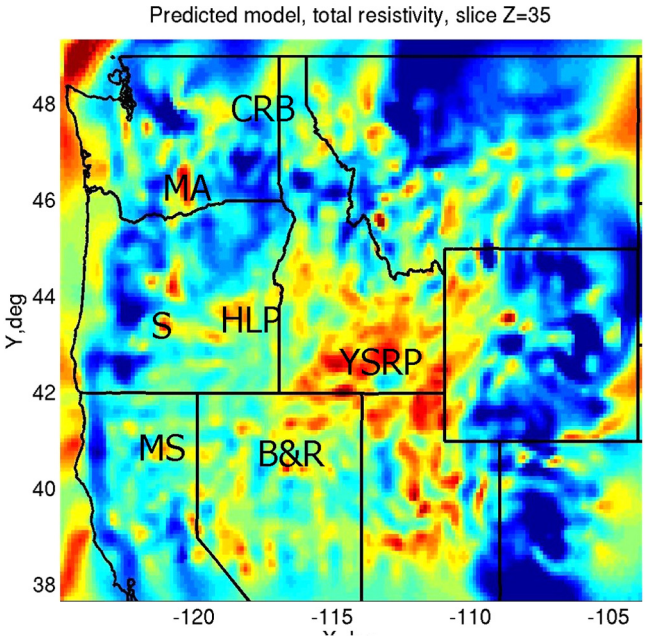

Fig. 9. Horizontal cross section at depth of 35 km obtained with MT inversion.

Fig. 11 presents the vertical sections of the geoelectrical model for the profile AA', starting from the northern Basin and Range (BR), proceeding along the Snake River Plain (see Fig. 5) over the traces of the path of the North American plate over the Yellowstone hotspot. The Yellowstone hot conductive layer is clearly imaged in the geoelectrical model as a low-resistivity (~ 1–5 Ohm-m) anomaly (YH). Similar conductive feature was previously identified by Zhdanov et al. (2012) using a subset of EarthScope MT stations located over the area surrounding Yellowstone National Park. This observation correlates well with the seismic models of Obrebski et al. (2010, 2011), which are characterized by the lower velocity anomaly at the shallow, elongated part of the plume-like layer extending to depths of about ~300 km. Both of these observations are consistent with the presence of partial melt, which decreases the seismic velocity and increases the electric conductivity. As was discussed in Zhdanov et al. (2011, 2012), the low resistivity of the conductive structure (of an order of 1–5 Ohm-m) is comparable to the resistivity of silicate melts determined from laboratory experiments (Pommier et al., 2008), and it is explained by a high temperature partial melt, or by the effect of highly saline fluids present in magmatic processes. We should note that the geoelectrical model of Meqbel et al. (2013) along their line MM' indicates a deep conductive feature similar to ours, however, shifted to the northeast from the location resolved by our model and not peaking out.

The upper crustal conductors tend to have a shielding effect on resolution of the deeper mantle conductors, and there has been some discussion about the validity of the resolved anomalies below about 200 km depth. To evaluate the effective depth resolution of our EarthScope models, we conducted a modeling and inversion experiment, where we calculated impedances of a model, which consisted of the first vertical 100 km of the resolved full impedance EarthScope model, and included a 10 Ohm-m conductive anomaly below 200 km in an otherwise homogeneous 100 Ohm-m background. In Fig. 12 a, we show a vertical cross section of the first model which has a 200 km thick 10 Ohm-m conductor between 200 and 400 km depth. This conductor covers the whole domain in the north–south direction and area from −106 W to −122 W longitudinally. Fig. 12 b shows the inversion result using coarse, horizontal 25 × 25 km cell size grid with 48 logarithmically increasing vertical layers. Notice that, the deep conductor is resolved better in the eastern part of the cross section, where there are only weak upper crustal conductors. The central area, which has numerous strong upper crustal conductors, also resolves the deeper conductor quite well, albeit at lesser contrast. Fig. 13 a shows a vertical cross section of the initial model at 50 km. The upper crustal conductors are the most prominent in the south central area. Fig. 13b shows the inversion result at a depth of 300 km. The deep conductor is apparent in its entirety, although the anomaly is weaker in the area under the strongest crustal conductors.

Finally, in the resolved EarthScope geoelectrical model, the deep conductor seems to bottom out at around 400 km depth. In order to evaluate if this is due to the true anomaly or due to lack of sensitivity below 400 km, we have considered another model, the same as previously described, except that the deep anomaly was extended from 200 to 500 km and the background was set to 10 Ohm-m below the bottom of the modeling domain at 500 km. A vertical cross section through this model is shown in Fig. 14 a. Fig. 14b shows the inversion result at the same vertical cross section. In the inversion, we assumed a homogeneous half-space with

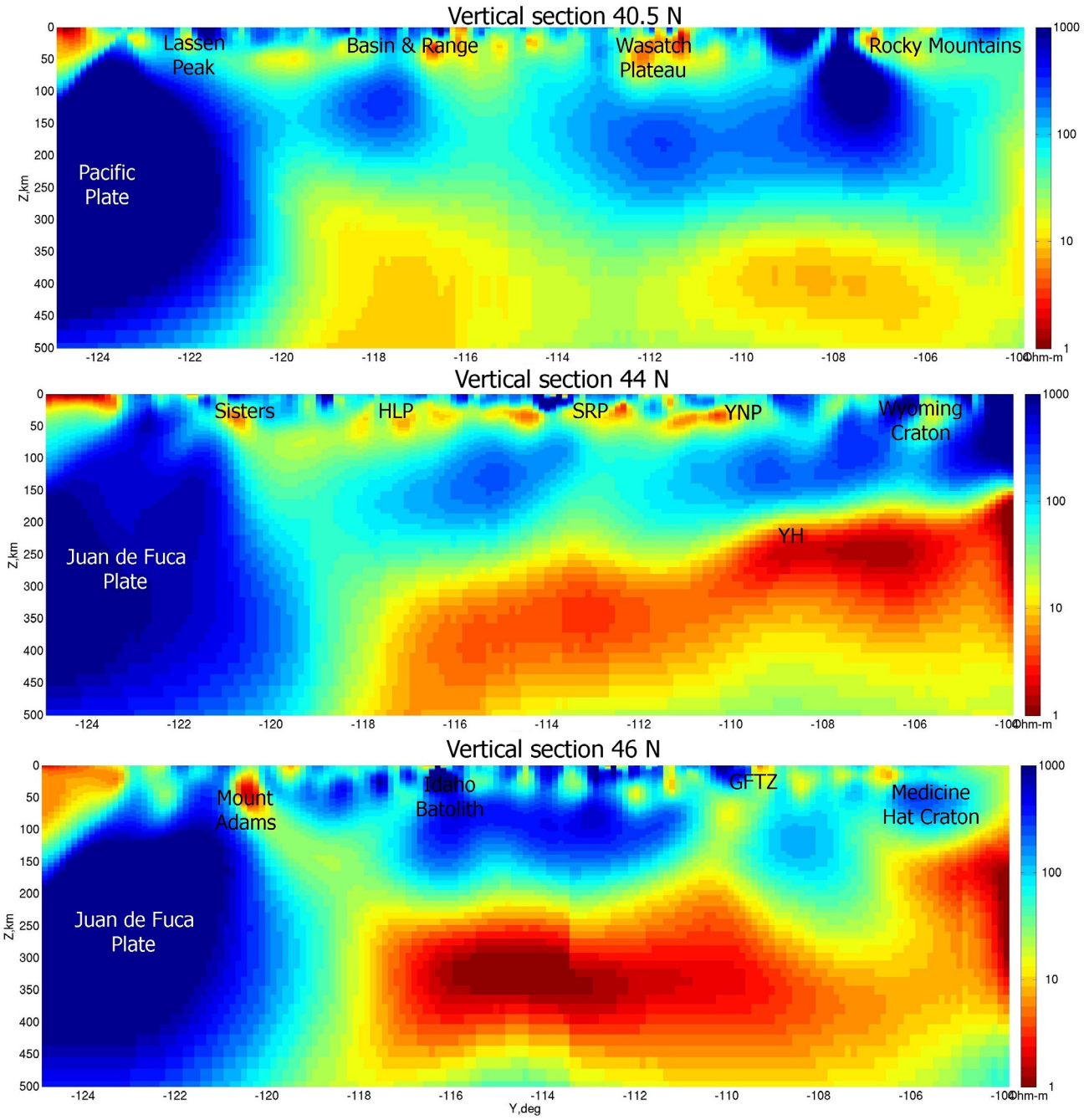

Fig. 10. Vertical cross sections of the EarthScope resistivity model obtained from the MT inversion.

100 Ohm-m background as in all previous inversions. Note that, the deep conductor anomaly is not resolved below 400 km depth, which suggests that the data do not have sensitivity below ca. 400 km depth.

7. Conclusions

We have presented a detailed description of a method of large-scale inversion of magnetotelluric (MT) data based on integral equation forward modeling and a variable sensitivity domain. This method is implemented as a parallel MT inversion code, which can be used for inversion of the data collected by hundreds of MT stations into the conductivity distribution over the large-scale grid with millions of discretization cells. A possibility of considering large-scale inversion grid is based on a concept of moving and variable sensitivity domain, which exploits the physical fact that each MT station has limited sensitivity to the conductivity distribution, which also varies with frequency.

We have applied our inverson approach to the EarthScope MT data acquired to the end of 2011 over the northwestern United States. In agreement with other MT inversion studies (Bedrosian and Feucht, 2013; Meqbel et al., 2013), our inverse geoelectrical model shows a resistive structure associated with the Juan de Fuca slab subducting beneath the Precambrian northwestern United States, and the conductive anomalies characterizing the partially melted material above the subducting slab. The geoelectrical model also contains several prominent conductive features, such as conductive lineaments beneath the High Lava Plains and the

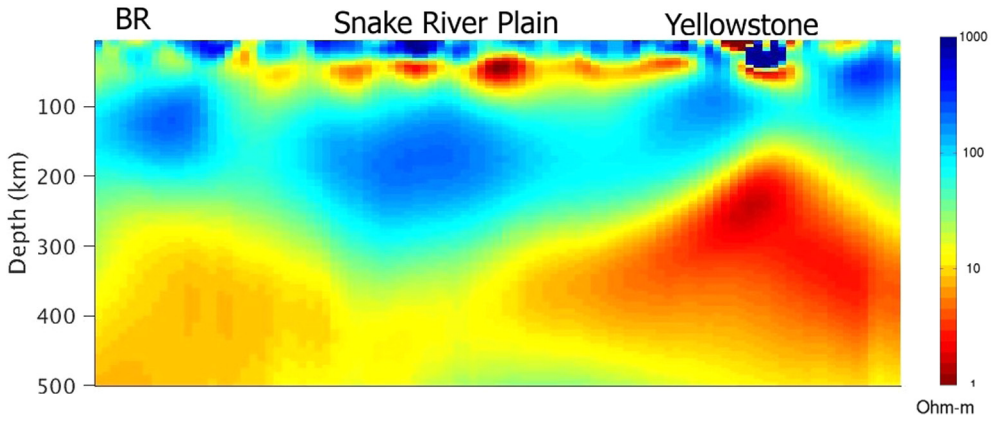

Fig. 11. Vertical cross section along AA' profile obtained with MT inversion.

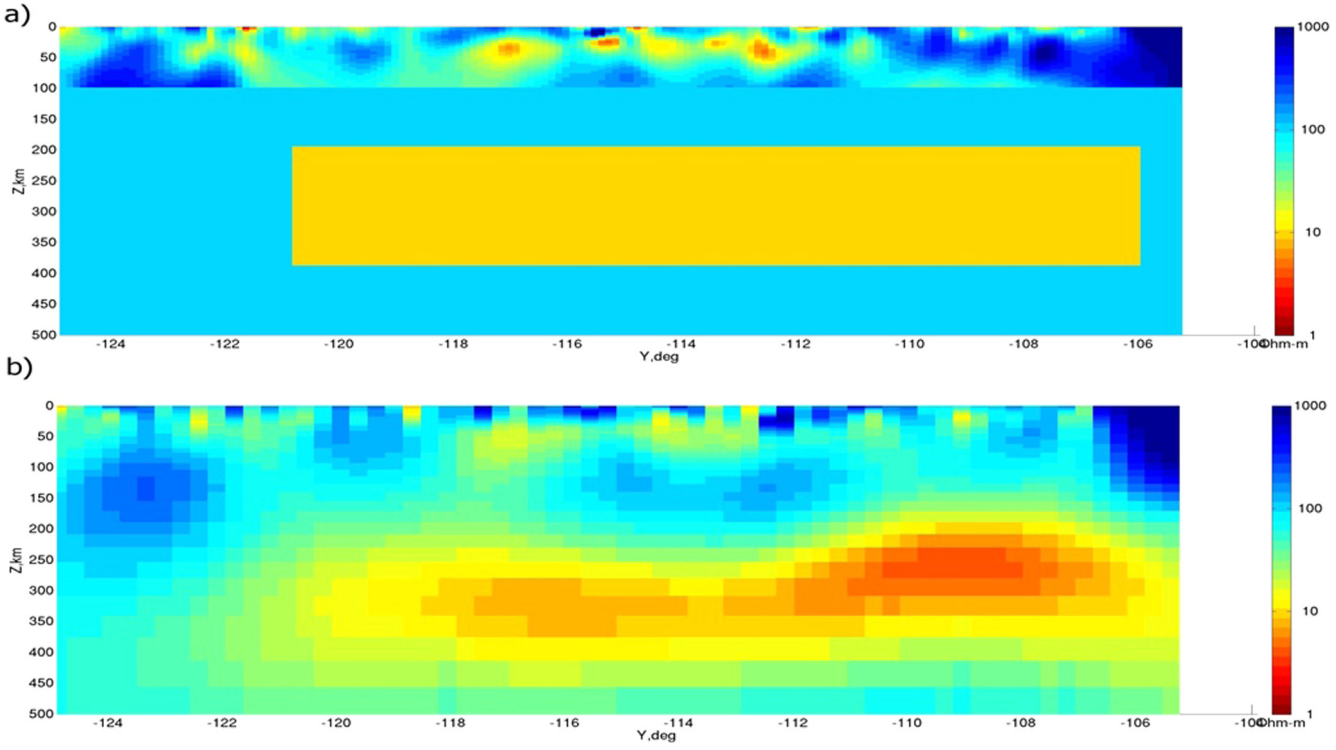

Fig. 12. Vertical cross section of a deep conductor model (a) and the inverted result (b).

Snake River Plain, conductivity anomalies extending beneath the Columbia River basalts and Basin and Range, the conductive mantle layer of the Yellowstone hotspot, and extensive areas of low resistivity in the upper mantle and in the low crust. These results also generally correlate well with the P-wave and S-wave velocity models obtained from seismic tomography. We have also determined that our inversion method with the MT data used is sensitive to about 400 km depth and reveals extensive mantle conductors below 200 km.

We should note that, one of the major goals of this paper was to make the results of inversion of the EMscope data available to a wide international geological and geophysical community by providing a digital inverse model as a Supplementary Material, which everybody can digest, analyze, and interpret. We believe that the results of the EMScope project should exist not only in the form of the observed MT data, but in a form of the corresponding geoelectrical models extracted from these data.

We believe that the geoelectrical model obtained from our 3D MT inversion provides important complementary information to the previously published geoelectrical and seismic models, and will help to better understand the complex tectonic processes responsible for the formation of the unique geological features of the North America subduction zone. The focus of future research should be on the integrated interpretation of seismic, electromagnetic, gravity, magnetic, and geothermal data, which would reduce the ambiguity of geophysical inversion.

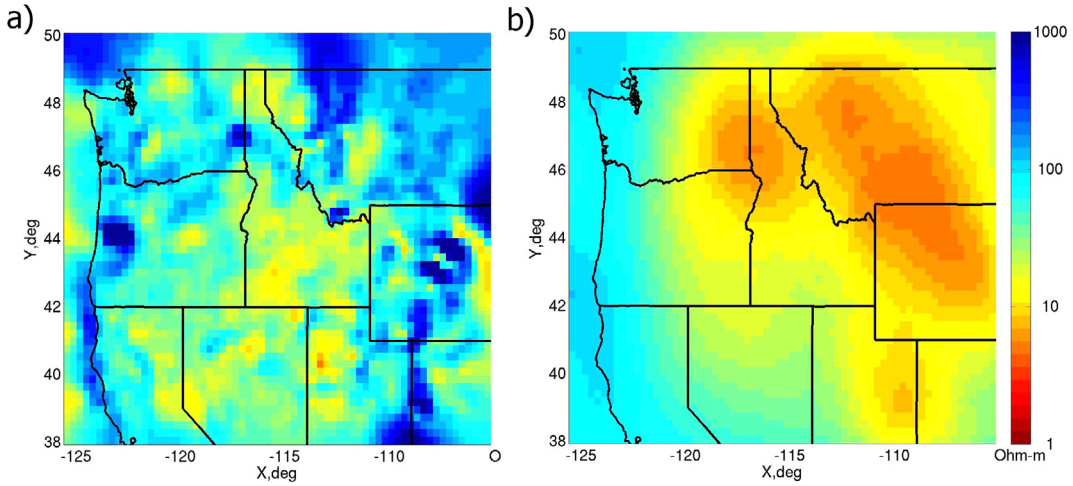

Fig. 13. a) Horizontal cross section of deep conductor model at 50 km showing the areas of upper crustal conductors in the south central part of the domain; b) Horizontal cross section of the inverted result at 300 km depth showing the resolved deep conductor. Notice the conductor resolution is weaker in the south central part, which is shielded the most by the upper crustal conductors.

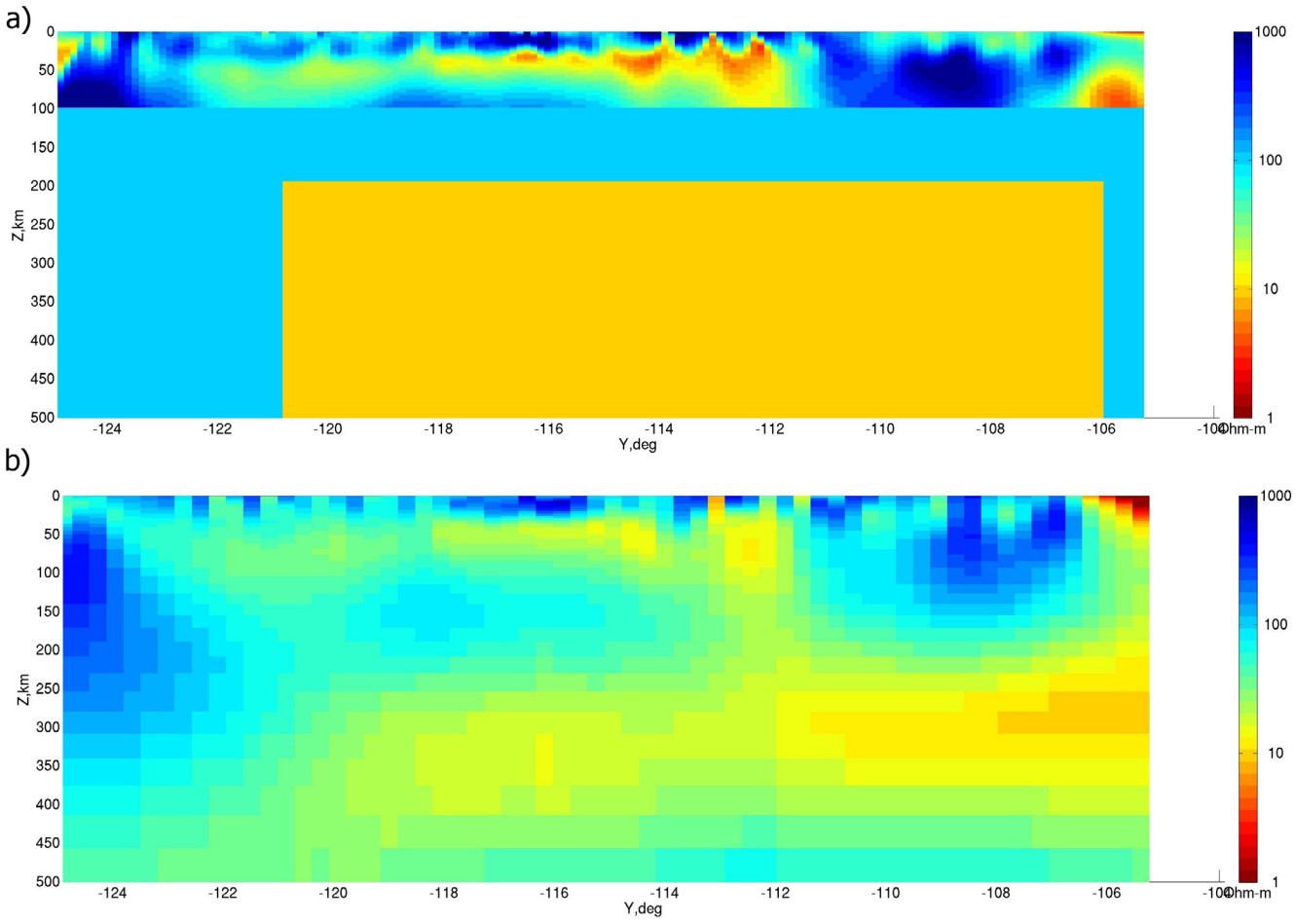

Fig. 14. Vertical cross section of a deep conductor model with conductor going to the bottom of the domain (a) and the inverted result (b).

Acknowledgments

The authors acknowledge the support of the University of Utah Consortium for Electromagnetic Modeling and Inversion (CEMI).

The MT data were acquired by the Incorporated Research Institutions for Seismology (IRIS) as part of the operation of the USArray. Data used in this study were made available through EarthScope (www.earthscope.org; EAR-0323309), supported by the National Science Foundation.

We also acknowledge allocation of computer time provided by the University of Utah's Center for High Performance Computing (CHPC) and the Texas Advanced Computing Center (TACC). We also

acknowledge TechnoImaging for support of this research. We further thank graduate students Marie Green, Muran Han, and Yue Zhu for assistance with some of the model studies.

Appendix A. Supplementary data

Supplementary data associated with this article can be found, in the online version, at http://dx.doi.org/10.1016/j.pepi.2017.06.003.

References

Abubakar, A., van den Berg, P.M., 2004. Iterative forward and inverse algorithms based on domain integral equations for three-dimensional electric and magnetic objects. J. Comput. Phys. 195, 236–262.

Avdeev, D., Avdeeva, A., 2009. 3d magnetotelluric inversion using limited-memory quasi-newton optimization. Geophysics 74, F45–F57.

Avdeev, D.B., Kuvshinov, A.V., Pankratov, O.V., Newman, G.A., 2002. Three-dimensional induction logging problems, Part i: an integral equation solution and model comparisons. Geophysics 67, 413–426.

Bedrosian, P.A., Feucht, D.W., 2013. Structure and tectonics of the northwestern united states from earthscope usarray magnetotelluric data. Earth Planet. Sci. Lett. 402, 275–289.

Berdichevsky, M.N., Zhdanov, M.S., 1984. Advanced Theory of Deep Geomagnetic Sounding. Elsevier.

Carlson, R.W., Grove, T.L., Donnelly-Nolan, J.M., 2008. Concentrating the slab-fluid input to newberry volcano. Geochim. Cosmochim. Acta 72, A136.

Cox, L.H., Wilson, G.A., Zhdanov, M.S., 2010. 3d inversion of airborne electromagnetic data using a moving footprint. Explor. Geophys. 41, 250–259.

Čuma, M., Zhdanov, M.S., Yoshioka, K., 2013. Parallel integral equation 3d (pie3d) 2013. In: Proceedings of the Consortium for Electromagnetic Modeling and Inversion Annual Meeting.

Endo, M., Čuma, M., Zhdanov, M.S., 2008. Multigrid ie method for large-scale models with inhomogeneous background. J. Geophys. Eng. 5, 438–447.

Endo, M., Čuma, M., Zhdanov, M.S., 2009. Large-scale electromagnetic modeling for multiple inhomogeneous domains. Commun. Comput. Phys. 21, 269–289.

Fouch, M.J., 2012. The yellowstone hotspot: plume or not? Geology 40, 479–480.

Hohmann, G.W., 1975. Three-dimensional induced polarization and electromagnetic modeling. Geophysics 40, 309–324.

Hursán, G., Zhdanov, M.S., 2002. Contraction integral equation method in three-dimensional electromagnetic modeling. Radio Sci. 37, 1089.

James, D.E., Fouch, M.J., Carlson, R.W., Roth, J.B., 2011. Slab fragmentation, edge low and the origin of the yellowstone hotspot track. Earth Planet. Sci. Lett. 311, 124–135.

Meqbel, N.M., Egbert, G.D., Wannamaker, P.E., Kelbert, A., Schultz, A., 2013. Deep electrical resistivity structure of the northwestern u.s. derived from 3-d inversion of usarray magnetotelluric data. Earth Planet. Sci. Lett. 402, 290–304.

Obrebski, M.R., Allen, R.M., Pollitz, F., Hung, S.H., 2011. Lithosphere–asthenosphere interaction beneath the western united states from the joint inversion of body-wave traveltimes and surface-wave phase velocities. Geophys. J. Int. 185, 1003–1021.

Obrebski, M.R., Allen, R.M., Xue, M., Hung, S.H., 2010. Slab-plume interaction beneath the pacific northwest. Geophys. Res. Lett. 37, L14305.

Patro, P.K., Egbert, G.D., 2008. Regional conductivity structure of cascadia: Preliminary results from 3d inversion of usarray transportable array magnetotelluric data. Geophys. Res. Lett. 35, L20311.

Pommier, A., Gaillard, F., Pichavant, M., Scaillet, B., 2008. Laboratory measurements of electrical conductivities of hydrous and dry mt. vesuvius melts under pressure. J. Geophys. Res. 113, B05205.

Raiche, A.P., 1974. An integral equation approach to three-dimensional modelling. Geophys. J. Int. 36, 363–376.

Roth, J.B., Fouch, M.J., James, D., Carlson, W., 2008. Three-dimensional seismic velocity structure of the northwestern united states. Geophys. Res. Lett. 35, L15304.

Schmandt, B., Humphreys, E., 2010. Complex subduction and small-scale convection revealed by body-wave tomography of the western united states upper mantle. Earth Planet. Sci. Lett. 297, 435–445.

Schmandt, B., Humphreys, E., 2011. Seismically imaged relict slab from the 55 ma siletzia accretion to the northwest united states. Geology 39, 175–178.

Schutt, D.L., Dueker, K., 2008. Temperature of the plume layer beneath the yellowstone hotspot. Geology 36, 623–626.

Schutt, D.L., Dueker, K., Yuan, H., 2008. Crust and upper mantle velocity structure of the yellowstone hot spot and surroundings. J. Geophys. Res. 113, B03310.

Smith, B.S., Jordan, M., Steinberger, B., Puskas, C., Farrell, J., Wait, G., Husen, S., Chang, W.L., O'Connell, R.J., 2009. Geodynamics of the yellowstone hotspot and mantle plume: seismic and gps imaging, kinematics, and mantle flow. J. Volcanol. Geoth. Res. 188, 26–56.

Smith, W.H.F., Sandwell, D., 1997. Global seafloor topography from satellite altimetry and ship depth soundings. Science 277, 1956–1962.

Stanley, W.D., Boehl, J.E., Bostick, F.X., Smith, H.W., 1977. Geothermal significance of magnetotelluric sounding of the eastern snake river plain – yellowstone region. J. Geophys. Res. 82, 2501–2514.

Tabarovsky, L.A., 1975. Application of integral equation method to geoelectrical problems. Nauka.

Tikhonov, A.N., Arsenin, V.Y., 1977. Solution of Ill-posed Problems. V.H Winston and Sons.

Waite, G.P., Schutt, D., Smith, R.B., 2005. Models of lithosphere and asthenosphere anisotropic structure of the yellowstone hot spot from shear wave splitting. J. Geophys. Res. 110, B11304.

Wannamaker, P.E., 1991. Advances in three-dimensional magnetotelluric modeling using integral equations. Geophysics 56, 1716–1728.

Wannamaker, P.E., Booker, J.R., Filloux, J.H., Jones, A.G., Jiracek, G.R., Chave, A.D., Tarits, P., Waff, H.S., Egbert, G.D., Young, C.T., Stodt, J.A., Martinez, M.G., Law, L. K., Yukutake, T., Segawa, J.S., White, A., Green Jr., A.W., 1989. Magnetotelluric observations across the Juan de Fuca Subduction System in the EMSLAB Project. J. Geophys. Res. 94, 14111–14125.

Weidelt, P., 1975. Electromagnetic induction in three-dimensional structures. J. Geophys. 41, 85–109.

Xiong, Z., 1992. Electromagnetic modeling of 3-d structures by the method of system iteration using integral equations. Geophysics 57, 1556–1561.

Zhdanov, M.S., 2002. Geophysical inverse theory and regularization problems. Elsevier.

Zhdanov, M.S., 2009. Geophysical Electromagnetic Theory and Methods. Elsevier.

Zhdanov, M.S., 2015. Inverse Theory and Applications in Geophysics. Elsevier.

Zhdanov, M.S., Gribenko, A., Čuma, M., Green, A.M., 2012. Geoelectrical structure of the lithosphere and asthenosphere beneath the northwestern united states. J. Geol. Geosci. 1, 1–6.

Zhdanov, M.S., Lee, S.K., Yoshioka, K., 2006. Integral equation method for 3-d modeling of electromagnetic fields in complex structures with inhomogeneous background conductivity. Geophysics 71, G333–G345.

Zhdanov, M.S., Smith, R.B., Gribenko, A., Čuma, M., Green, A.M., 2011. Three-dimensional inversion of large-scale earthscope magnetotelluric data based on the integral equation method: geoelectrical imaging of the yellowstone conductive mantle plume. Geophys. Res. Lett. 38, L08307.